DIRECT NUMERICAL SIMULATION OF A HYPERSONIC BOUNDARY LAYER IN CHEMICAL NON-EQUILIBRIUM

D. Passiatore[(1)], L. Sciacovelli[(2)], P. Cinnella[(3)] and G. Pascazio[(4)]

[(1)]*Politecnico di Bari, DMMM, via Re David 200, 70125 Bari, Italy, donatella.passiatore@poliba.it*

[(2)]*Arts et Métiers ParisTech, DynFluid Laboratory, 151 bd. de l'Hôpital, 75013 Paris, France, luca.sciacovelli@ensam.eu*

[(3)]*Sorbonne Université, Institut Jean Le Rond d'Alembert , 4 Place Jussieu, 75005 Paris, France, paola.cinnella@sorbonne-universite.fr*

[(4)]*Politecnico di Bari, DMMM, via Re David 200, 70125 Bari, Italy, giuseppe.pascazio@poliba.it*

ABSTRACT

The influence of high-enthalpy effects in hypersonic, spatially developing boundary layers is investigated by means of direct numerical simulations. The flow of a reacting mixture of nitrogen and oxygen over a flat plate at Mach 10, previously investigated in the literature using linear stability theory (LST), is simulated using a computational domain encompassing the laminar, transitional, and turbulent regimes. Transition is triggered by forcing Mack's second mode through suction and blowing at the wall. In the laminar region, the solution matches reasonably well the locally self-similar profiles, computed under chemical non-equilibrium assumptions. Strong dissociation phenomena are observed, due to the high temperatures reached close to the (uncooled) plate surface. The transitional regime is investigated by means of modal analysis. Despite the significant chemical activity, the results confirm the classical transition scenario for high-Mach number boundary layers, for which the second-mode resonance is the main mechanism responsible for turbulent breakdown. In the turbulent region, first- and second-order statistics reveal that chemical reactions do not modify significantly dynamic quantities such as velocity and Reynolds stress profiles, but greatly affect thermal properties, due to their endothermic nature. For the configuration at hand, chemical dissociation is slower than the characteristic time-scale of the flow, and the peak of chemical activity is located in the viscous sublayer, leading to mild modifications of the turbulent field compared to a frozen-chemistry model.

1. INTRODUCTION

The investigation of turbulent hypersonic flows is a major subject when dealing with planetary atmosphere reentries or vehicles capable of flying at hypersonic speed in the atmosphere. Recently, new vehicle concepts involving hypersonic flight are arousing interest not only in the defense and military fields, but also in the areas of spatial tourism and trans-atmospheric flights. The accurate prediction of boundary layer phenomena, such as laminar-to-turbulent transition, near-wall turbulence, wall friction and heat flux is of utmost importance in order to improve the design of hypersonic vehicles. Moreover, the amount of energy present in these specific configurations can cause vibrational excitation of the gas molecules and chemical reactions (with characteristic times similar to those of the fluid motion), giving rise to nonequilibrium thermochemical states. Such high-enthalpy effects have a strong impact on aerodynamic performances and heat transfer rates, but may also affect transition and turbulence dynamics [6]. Despite the enormous progress realized so far, high-speed aerodynamics and aerothermodynamics constitute some of the areas where improvements need to be made. Carrying out physical experiments in the working conditions of interest is generally a costly (sometimes unfeasible) task, given the difficulty in reproducing such critical configurations [2]. To palliate the lack of experimental data, it is possible to carry out scale-resolving numerical simulations, such as Large-Eddy Simulations (LES) or Direct Numerical Simulations (DNS), at least in a range of moderate Reynolds numbers. In particular, DNS ensures the proper resolution of the whole spectrum of active temporal and spatial scales, without any hypothesis nor modeling assumption, allowing to avoid the introduction of turbulence models not tailored (and thus not enough reliable) for hypersonic flows [29]. Despite the high computational cost of DNS, the generation of high-fidelity databases for out-of-

equilibrium, high-speed flows is therefore of great importance for understanding the underlying physical mechanisms and improving the existing turbulence models.
There exist limited DNS studies on turbulent, hypersonic boundary layers. For instance, Duan *et al.* [9, 7] performed DNS of temporally-evolving, zero-pressure-gradient turbulent boundary layers in the high-Mach regime and varying wall temperatures; whereas Mach numbers up to 20 were considered from Lagha *et al.* [20]. These configurations, however, do not exhibit high-temperature effects due to the cryogenic free-stream conditions. A comparative study between low- and high-enthalpy, reactive boundary layers was performed subsequently [8], although moderate temperature values were imposed at the wall (≈ 2400). Recently, more attention has been paid to hypersonic, cold-wall boundary layers in spatially-evolving configurations [31, 17].
The objective of the current paper is to assess the influence of strong chemical activity, caused by hypersonic conditions, on wall-bounded turbulent flows. Specifically, we aim at generating a new DNS database of high-enthalpy, spatially-developing turbulent boundary layers. The current analysis encompasses the laminar, transitional and fully turbulent regime. Free-stream conditions were chosen such that chemical reactions are triggered by the high near-wall temperature values. A nominal Mach number equal to M_∞=10 and a wall temperature computed under adiabatic condition are considered. These conditions have been widely used in the past for stability studies [23, 25, 24]. The present DNS study aims at providing further insights on the complete transition scenario, broadening the existing knowledge on the purely transitional regime to the fully turbulent one.
The paper is structured as follows. The governing equations, the numerical method and the simulation set-up are described in Section 2. Numerical results are presented in Section 3. After a brief investigation on the laminar flow regime, breakdown to turbulence is carefully scrutinized by means of spectral and modal analyses; afterwards, an overview of the main statistical turbulent quantities is provided. Conclusions and future works are drawn in Section 4.

2. METHODOLOGY

2.1 Governing equations

Flows under investigation are governed by the compressible Navier–Stokes equations for multicomponent, chemically-reacting gases, which read in differential form as:

$$\frac{\partial \rho}{\partial t} + \frac{\partial \rho u_j}{\partial x_j} = 0 \tag{1}$$

$$\frac{\partial \rho u_i}{\partial t} + \frac{\partial \left(\rho u_i u_j + p\delta_{ij}\right)}{\partial x_j} = \frac{\partial \tau_{ij}}{\partial x_j} \tag{2}$$

$$\frac{\partial \rho E}{\partial t} + \frac{\partial \left[(\rho E + p)\, u_j\right]}{\partial x_j} = \frac{\partial (u_i \tau_{ij} - q_j)}{\partial x_j} - \frac{\partial}{\partial x_j}\Big(\sum_{n=1}^{N} \rho_n u_{nj}^D h_n\Big) \tag{3}$$

$$\frac{\partial \rho_n}{\partial t} + \frac{\partial \rho_n u_j}{\partial x_j} = -\frac{\partial \rho_n u_{nj}^D}{\partial x_j} + \dot{\omega}_n \tag{4}$$

being $\rho = \sum_{n=1}^{N} \rho_n$ the mixture density, N the total number of species, u_i the velocity vector components, p the pressure, δ_{ij} the Kronecker symbol and τ_{ij} the viscous stress tensor, defined as

$$\tau_{ij} = \mu\left(\frac{\partial u_i}{\partial x_j} + \frac{\partial u_j}{\partial x_i}\right) - \frac{2}{3}\mu \frac{\partial u_k}{\partial x_k}\delta_{ij}, \tag{5}$$

with μ the mixture dynamic viscosity. Moreover, $E = e + \sum_{n=1}^{N} h_n^f Y_n + \frac{1}{2} u_i u_i$ denotes the total chemical energy, with e the specific internal energy, h_n^f and $Y_n = \rho_n/\rho$ the n-th species enthalpy of formation and mass fraction, respectively; q_j represents the heat flux modelled by means of the Fourier law, $q_j = -\lambda \frac{\partial T}{\partial x_j}$, λ being the mixture thermal conductivity and T the temperature. Lastly, u_{nj}^D, h_n, and $\dot{\omega}_n$ are the n-th species diffusion velocity (defined hereafter), specific enthalpy and rate of production, respectively. The code solves the mixture density and $N-1$ species conservation equations, the N-th species being computed as $\rho_N = \rho - \sum_{n=1}^{N-1} \rho_n$. In these simulations, the N-th species is Nitrogen (see eq. (8)) since it keeps the largest mass fraction throughout the computational domain. Each species is assumed to behave as a perfect gas; Dalton's pressure mixing law leads then to the mixture pressure equation equation of state:

$$p = \sum_{n=1}^{N} p_n = \mathscr{R}\rho T \sum_{n=1}^{N} \frac{Y_n}{W_n} = T \sum_{n=1}^{N} \rho_n R_n \tag{6}$$

being R_n and W_n the gas constant and molecular weight of the n-th species, respectively, and $\mathscr{R} = 8.314$ J/mol K the universal constant of gases. The thermodynamic properties of high-T air species are computed considering the contributions of translational, rotational and vibrational modes for each species [14]. An iterative Newton's method is used to compute T given the mixture internal energy and the species partial densities.
With regard to the transport coefficients, pure species' viscosity and thermal conductivity are computed using Blottner's model and Eucken's formula, respectively [4]; the corresponding mixture properties are evaluated by means of Wilke's mixing rule. The diffusion velocities

are given by Fick's law

$$u_{nj}^{D}\rho_n = -\rho D_n \frac{\partial Y_n}{\partial x_j} + \rho_n \sum_{n=1}^{N} D_n \frac{\partial Y_n}{\partial x_j}, \qquad (7)$$

where D_n is an equivalent diffusion coefficient of species n into the mixture, computed as in [16]. The second term in the right-hand-side of eq. (7) represents a correction needed to recover total mass conservation (see Ref. [28]). Air is modeled as a five-species mixture of N_2, O_2, NO, O and N. The chemical source terms $\dot{\omega}_n$ are computed following Park's model [27], for which the species interact with each other through a 17-reaction mechanism:

$$\begin{aligned} N_2 + M &\Longleftrightarrow 2N + M \\ O_2 + M &\Longleftrightarrow 2O + M \\ NO + M &\Longleftrightarrow N + O + M \\ N_2 + O &\Longleftrightarrow NO + N \\ NO + O &\Longleftrightarrow N + O_2 \end{aligned} \qquad (8)$$

where M represents any of the five species considered. Lastly, the reaction rates are modeled by means of Arrhenius' law.

2.2 Numerical methods

The governing equations are approximated using high-order finite-difference schemes. The convective fluxes are discretized by means of tenth-order schemes on 11-points stencils, whereas standard fourth-order schemes are used for viscous fluxes. The discretization method is supplemented with a higher-order extension of Jameson's adaptive artificial dissipation [19]. A highly-selective shock sensor, built on a combination of the original Ducros' extension [10] of Jameson's pressure-based sensor with the Bhagatwala & Lele modification [3] is used to trigger the shock-capturing term. Time integration is carried out by means of a third-order TVD Runge-Kutta scheme [15].

2.3 Simulation set-up

A boundary-layer over a semi-infinite flat plate is considered. The thermodynamic conditions are similar to those adopted in several stability studies (see Refs. [23, 18, 11, 24, 26]); specifically, the imposed free-stream values are M_∞=10, T_∞=350 K and p_∞=3596 Pa. Air in equilibrium at its free-stream conditions is prescribed (namely, $Y_{N_2} = 0.767082$ and $Y_{O_2} = 0.232918$, similar to Marxen *et al.* [24]). Adiabatic, non-catalytic boundary conditions are imposed at the wall. The domain is rectangular with even spacing in the streamwise (x) and spanwise (z) directions; in the wall-normal (y) direction, the following grid stretching is applied:

$$\frac{y(j)}{L_y} = (1-\alpha)\left(\frac{j-1}{n_y-1}\right)^3 + \alpha\frac{j-1}{n_y-1} \qquad (9)$$

Table 1: Parameters of the modes excited by the forcing function in equation (10): non-dimensional frequency ω_m, amplitude A_m and spanwise wave number β_m for the m-th mode.

N_{mode}	ω_m	A_m	β_m
1	1.71	0.05	0
2	0.855	2.50×10^{-3}	0
3	0	2.50×10^{-3}	+0.2
4	0	2.50×10^{-3}	+0.4
5	0	2.50×10^{-3}	+0.6
6	1.71	2.50×10^{-3}	-0.2
7	1.71	2.50×10^{-3}	+0.2
8	0.855	2.50×10^{-3}	-0.2
9	0.855	2.50×10^{-3}	+0.2
10	1.71	2.50×10^{-3}	-0.4
11	1.71	2.50×10^{-3}	+0.4
12	1.71	2.50×10^{-3}	-0.6
13	1.71	2.50×10^{-3}	+0.6

where L_y and n_y denote the domain length and the number of grid points along y-direction, respectively; $j \in [1, n_y]$ and α=0.13. The extent of the computational domain is $L_x \times L_y \times L_z = 8000\delta^*_{\text{in}} \times 320\delta^*_{\text{in}} \times 100\pi\delta^*_{\text{in}}$ (the inlet displacement thickness δ^*_{in} of the boundary layer being used as length scale) discretized with $N_x \times N_y \times N_z = 5520 \times 256 \times 240$ points. Locally self-similar profiles, computed under finite-rate chemistry assumptions, are prescribed at the inlet at a distance corresponding to Re_{δ^*}=6375 (Re_{δ^*} denoting the Reynolds number based on the displacement thickness). The derivation of the self-similar equations and their numerical solution are shown in the next section. A blowing and suction method, similar to the one used by Franko & Lele [12], is adopted to trigger transition to turbulence. Specifically, the suction-and-blowing function is imposed along a forcing strip located at $\text{Re}_{\delta^*} = 13880$ and reads:

$$\frac{v_w}{u_\infty} = f(x)g(z)\sum_{m=1}^{N_{\text{mode}}} A_m \sin(\omega_m t + \beta_m z), \qquad (10)$$

where $f(x)$ and $g(z)$ are two perturbation-modulation functions defined as in Franko & Lele [12] and A_m, $\omega_m = \widetilde{\omega}_m\delta^*_{\text{in}}/c_\infty$ and $\beta_m = \widetilde{\beta}_m\delta^*_{\text{in}}$ represent the amplitude, non-dimensional pulsation and spanwise wave number, respectively. Here, the superscript $\widetilde{(\bullet)}$ denotes the dimensional values and c_∞ the freestream speed of sound. The collection of forcing parameters for each mode are listed in table 1. Lastly, a sponge layer is applied near the inlet up to $35\delta^*_{\text{in}}$, to prevent abrupt distortions caused by the high Mach number. A sketch of the computational domain, starting downstream of the leading edge, is provided in fig. 1.

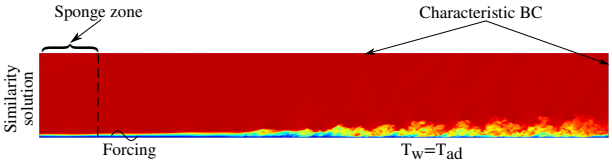

Figure 1: Sketch of computational domain.

2.4 Locally self-similar equations for reacting boundary layers

The imposition of a similarity solution at a given distance from the virtual origin of the plate allows one to avoid the numerical simulation of the plate leading edge, bypassing its singularity and reducing computational cost. Global self-similar solutions for high-T laminar boundary layers only exist in restricted cases, such as in presence of frozen or equilibrium chemistry assumptions [1]. Taking into account finite-rate chemistry, global similarity breaks down due to the the presence of source terms in the species equations. Nevertheless, it is possible to compute a locally (*i.e.*, x-dependent) self-similar solution, allowing the introduction of inlet profiles suitable for the configuration under investigation. Starting from the boundary-layer equations for steady, compressible, multicomponent, reacting, two-dimensional and zero-pressure-gradient flows, the following variable transformations are introduced (see Ref. [21] for more details):

$$\xi = \rho_e \mu_e U_e x = \xi(x), \quad \eta = \frac{U_e}{\sqrt{2\xi}} \int_0^y \rho dy = \eta(x,y),$$

where the subscript $(\bullet)_e$ denotes variables computed at the boundary layer edge. The definition of the streamfunction $\frac{\partial \psi}{\partial y} = \rho u$, $\frac{\partial \psi}{\partial x} = -\rho v$ and the equivalent expression in terms of transformed variables $\frac{\partial \psi}{\partial \xi} = \frac{1}{\sqrt{2\xi}} f(\eta)$, $\frac{\partial \psi}{\partial \eta} = \sqrt{2\xi} f'(\eta)$, with $f' = u/U_e$, allow to manipulate the boundary-layer equations obtaining the following formulation in the self-similar coordinate system:

$$\left(Cf''\right)' + ff'' = 0 \tag{11}$$

$$\left[\frac{\rho^2 D_n}{\rho_e \mu_e}\left(Y_n' - Y_n \sum_{i=1}^{NS} \frac{D_i}{D_n} Y_i'\right)\right]' + fY_n' + \frac{2\xi \dot{\omega}_n/\rho}{\rho_e \mu_e u_e^2} = 0 \tag{12}$$

$$\frac{T_e}{h_{0,e}}\left(\frac{C\lambda}{\mu}\theta'\right)' + fg' + \frac{u_e^2}{h_{0,e}} ff'f'' + \frac{u_e^2}{h_{0,e}}\left(Cf'f''\right)' + \left[\sum_{n=1}^{NS} \frac{h_n}{h_{0,e}} \frac{\rho^2 D_n}{\rho_e \mu_e}\left(Y_n' - Y_n \sum_{i=1}^{NS} \frac{D_i}{D_n} Y_i'\right)\right]' = 0 \tag{13}$$

Here, $g = h/h_{0,e}$ is the self-similar parameter for the enthalpy, $h_{0,e}$ being the edge stagnation enthalpy, $\theta = T/T_e$ and $C = \rho\mu/\rho_e\mu_e$ denotes the Chapman-Rubesin parameter. In case of frozen chemistry or chemical equilibrium, the ξ-dependent term in eq. (12) vanishes and the resulting equations become globally self-similar. The system (11)-(12) constitutes a two-point boundary value problem, subjected to the following boundary conditions:

$$f' = f = 0, \quad Y_n' = 0, \quad g' = 0 \quad \text{for} \quad \eta = 0$$

$$f' = 1, \quad Y_n = Y_{n,e}, \quad g = 1 - \frac{1}{2}\frac{u_e^2}{h_{0,e}} \quad \text{for} \quad \eta \to \infty,$$

which is easily integrated numerically by means of a globally-convergent Newton method.

3. RESULTS

After having reached a statistically steady state, time- and spanwise-averaged statistics are collected for approximately two turnover times with a sampling time interval of $\Delta t_s c_\infty/\delta^*_{in} = 3.45 \times 10^{-2}$. To carry out the spectral analysis, a selection of subvolumes of the computational domain is extracted at a sampling interval of $\Delta t_s c_\infty/\delta^*_{in} = 2.30 \times 10^{-1}$, corresponding exactly to sixteen snapshots per each period of the fundamental forcing harmonic. Figure 2 displays an instantaneous visualization of the boundary layer spatial evolution. The blowing and suction forcing, located near the inlet, triggers the turbulence breakdown and provides large transitional and turbulent zones to analyse. In the following, streamwise profiles are shown as a function of the nondimensional quantity $(x - x_0)/\delta^*_{in}$, x_0 being the distance from the leading edge. The inspection of the skin friction coefficient $C_f = \frac{2\overline{\tau}_w}{\rho_\infty u_\infty^2}$ (where $\overline{(\bullet)}$ denotes the Reynolds average), shown in fig. 3(a), reveals that the breakdown appears at $\approx 3000\delta^*_{in}$, whereas the fully turbulent region starts from $\approx 5000\delta^*_{in}$, *i.e.* from the streamwise location at which the downstream decrease of C_f begins.

3.1 Laminar regime

The laminar regime is analysed first. Figure 3(b) displays a close-up of C_f in the first part of the domain, along with the compressible extension of Blasius' laminar correlation, $C_f^{lam} = \frac{0.664}{\sqrt{Re_x}}\sqrt{\frac{\overline{\rho}_w \overline{\mu}_w}{\rho_\infty \mu_\infty}}$, and the locally self-similar solution at selected stations. It is worth noting that after the forcing strip (not visible in the figure), the evolution of C_f matches the laminar correlation, meaning that no mean-flow distortion has occurred yet. On the other hand, the similarity theory predicts slightly higher values of C_f; this gap is likely due to the presence of an external pressure gradient in the full Navier-Stokes equations, which is neglected in the self-similar ones. Similar slight discrepancies are present in the streamwise evolution of species mass fractions at the wall (fig. 4(a)). Overall, the numerical solution and the similarity theory are found to be in fair agreement. As the Reynolds number increases, the natural evolution of the boundary layer gives rise to

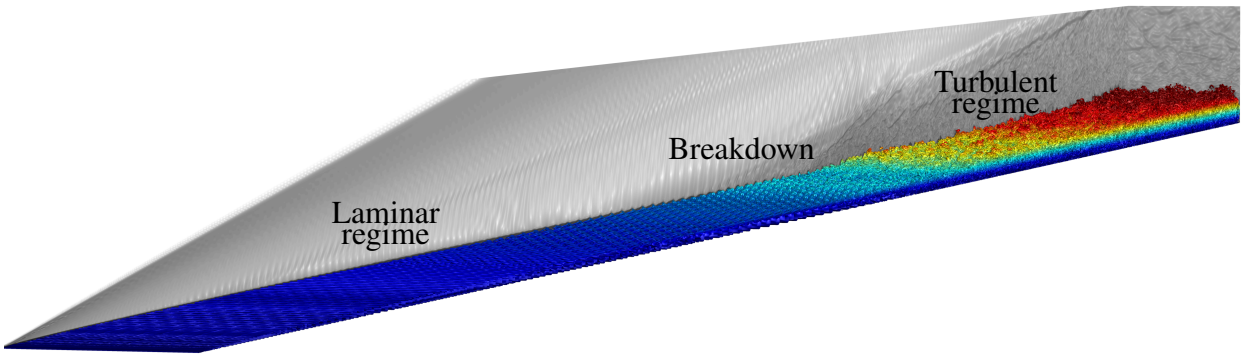

Figure 2: Instantaneous visualization of the computational domain: isosurface of Q-criterion coloured with the distance from the wall. On the back, Schlieren-like density contours showing the propagation of waves outside the boundary layer.

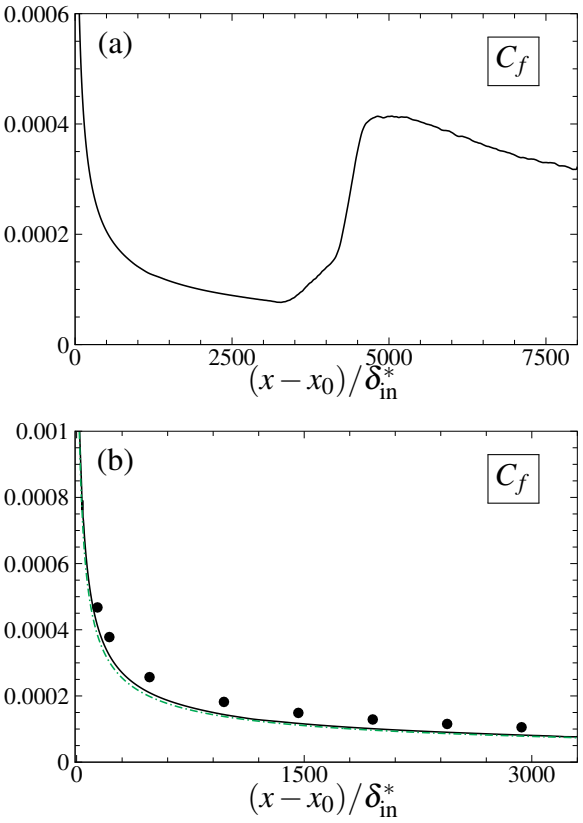

Figure 3: Streamwise evolution of skin friction coefficient C_f. (a) Entire domain and (b) zoom in the laminar region, along with the laminar correlation (-·-·-) and the locally self-similar solution (symbols).

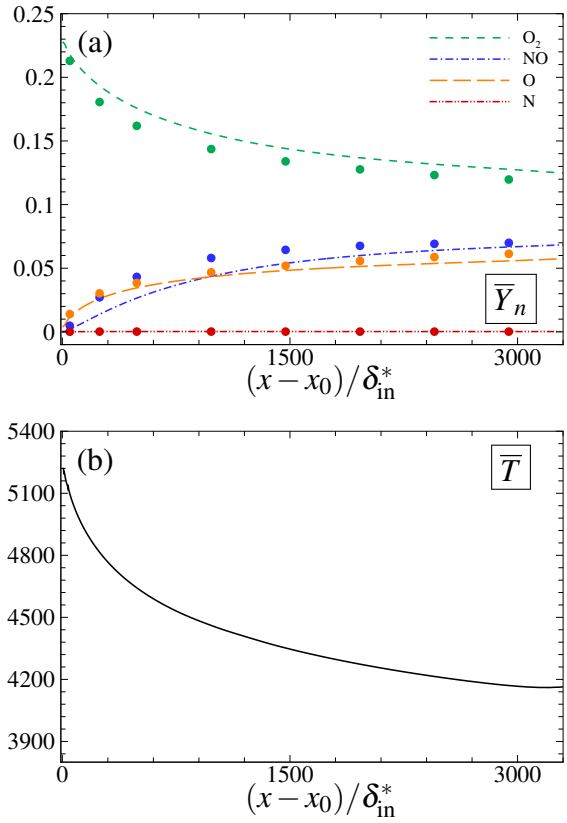

Figure 4: Streamwise evolution of (a) the mean species mass fractions at the wall, along with the locally self-similar solution (symbols), and (b) mean wall temperature [K]. In figure (a), N_2 is not shown being outside the displayed range.

a decreasing wall temperature profile (fig. 4(b)), in accordance with the locally self-similar trends (not shown). The temperatures values along the plate allow the activation of the exchange reactions; dissociation of O_2 starts and leads to the production of atomic oxygen and nitric oxide. Further downstream, the chemical activity slows down, indicating that the chemical time scales become much smaller than the flow residence time (as it will be shown later), resulting in a persisting chemical non-equilibrium composition.

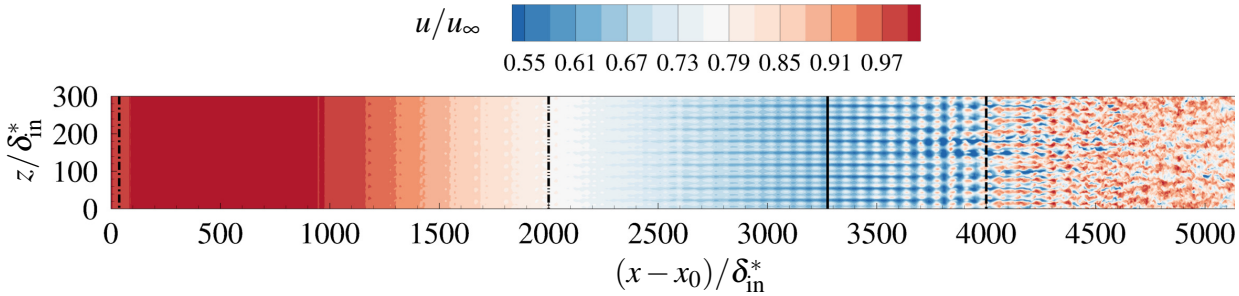

Figure 5: Instantaneous visualization of normalized velocity in a xz plane, extracted at $y/\delta^*_{in} = 13$. Four streamwise positions are marked, at $(x-x_0)/\delta^*_{in} = 36$, 2000, 3280 and 4000, the first one being the forcing strip.

3.2 Transitional regime

The nonlinear breakdown to turbulence is now investigated. The transition scenario is described by means of a modal analysis, which consists in evaluating the amplitude of excited modes through a spatio-temporal Fourier transform. The new coordinate system is then based on the angular frequency and spanwise wavenumber (ω, β). For the sake of simplicity, the angular frequency is normalized by 0.855 and the spanwise wave number by 0.2, corresponding to the couple (ω_9, β_9) in table 1. In previous works [12, 13], the amplitude of each mode is evaluated employing the modal energy, which takes into account both the kinetic and internal energy contributions. On the other hand, other references make use of the maximum amplitude of the streamwise velocity fluctuation [24]. The latter criterion is retained in this work for the modal growth analysis. To this aim, instantaneous velocity values are extracted along a cut of the computational domain in the y-direction, which follows the streamwise evolution of the wall-normal location at which the u-fluctuation peaks. A total number of 800 samples are considered. The maximum disturbance amplitude is then evaluated as $|u'|^2_{max} = |\widehat{u'}\widehat{u'}^*|/u^2_\infty$ (where $\widehat{(\bullet)}$ stands for the Fourier component and $(\bullet)^*$ denotes the complex conjugate) and results in a function of $(\omega/\omega_9, \beta/\beta_9, x)$. Figure 5 displays the normalized streamwise velocity in a xz plane, cut at the end of the transitional zone. The qualitative evolution of the disturbances shows that the footprint of three-dimensional modes starts to be visible at $(x - x_0)/\delta^*_{in} \approx 2500$, albeit they do not emerge significantly. This behavior underlines that the predominant mode in the first part of the domain is the two-dimensional Mack mode, excited with the strongest amplitude through suction and blowing (see tab. 1). Nonlinear effects lead to the growth of oblique and stationary modes and cause the development of streaks which, in this specific configuration, rapidly destabilize the flow and promote the breakdown to turbulence. This scenario occurs in the region $3000 < (x-x_0)/\delta^*_{in} < 4000$, corresponding to the slight kink in the C_f of figure 3(a), which indicates that a mean-flow distortion has occurred. To better understand this mechanism, frequency-wavenumber spectra are displayed in fig. 6 at the four selected locations marked in figure 5, the first one corresponding to the suction and blowing position. As expected, fig. 6(a) is in perfect

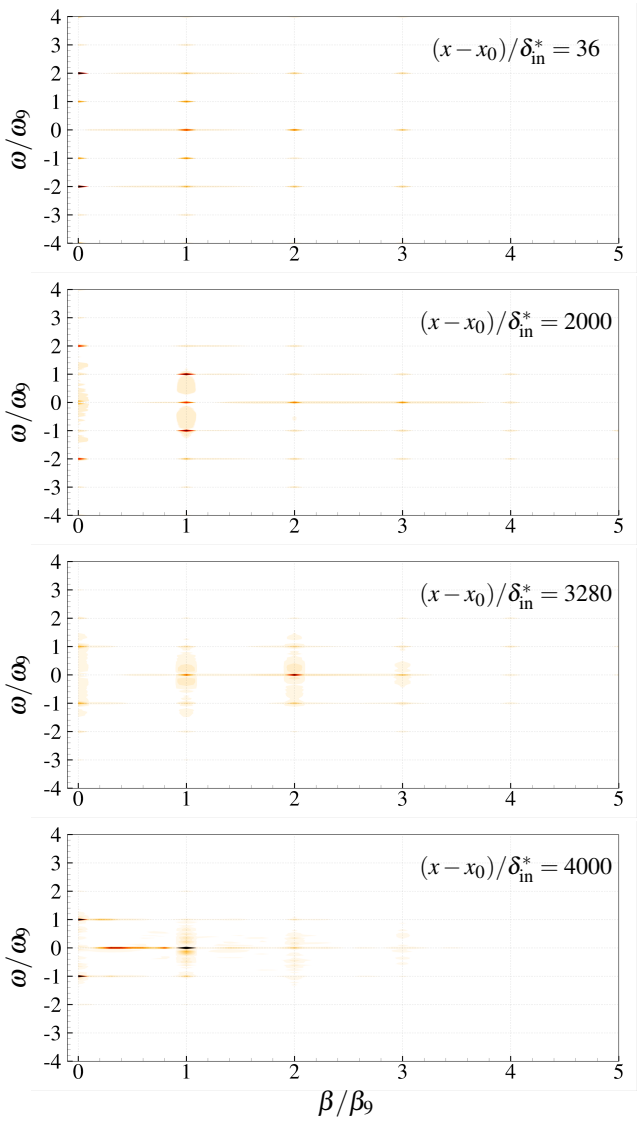

Figure 6: Frequency-wave number spectra at different streamwise positions.

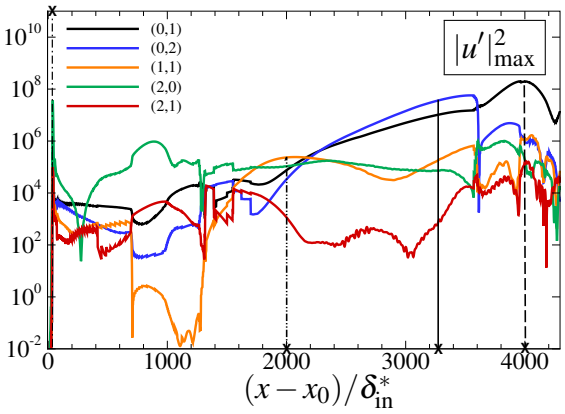

Figure 7: Streamwise developments of the maximum velocity disturbance amplitude, for the couples $(\omega/\omega_9, \beta/\beta_9)$ marked in the legend. Marked streamwise positions at $(x-x_0)/\delta^*_{in} = 36$, 2000, 3280 and 4000.

accordance with the modes excited by the forcing function, the couple (2,0) being the strongest in magnitude. Moving towards the successive streamwise location, the amplitude of sub-harmonics (1,1) and (-1,1) starts to increase; these modes are explicitly introduced in the forcing function but with an extremely low amplitude with respect to the primary harmonic, and are amplified by the flow as they move downstream. Finally, at the last two selected stations, exchange between various waves has led to the growth of the stationary waves (0,2) and (0,1), respectively. In order to follow the entire streamwise development, figure 7 shows the maximum velocity disturbance amplitude of selected modes. Initially, the mode (2,0) predominates over all the excited modes, but it rapidly decays and then saturates. At the same time, the sub-harmonic oblique wave (1,1) drops of several orders of magnitude first, and then becomes the most energetic mode at $(x-x_0)/\delta^*_{in} \approx 2000$. Downstream of this station, the streaks modes (0,1) and (0,2) start to emerge. The higher streak mode (0,2) initially dominates, but at later transition stages the principal stationary mode (0,1) overwhelms the former, leading to the breakdown and to the final saturation stage (not shown in the figure). The transition event is qualitatively similar to the second-mode breakdown of [12] for a $M_\infty = 6$ non-reacting boundary-layer. Late transition is typical of this scenario, since the stationary waves start to gain energy once the Mack mode saturates. We also observe that the present transition mechanism differs from wall-cooled boundary layers, in which early and persistent streaks are visible from the beginning of the transitional zone; here, the extremely high temperature results in late formation of the streaks which, by the way, remain the principal responsible for transition to turbulence.

Table 2: Numerical parameters of the selected locations for turbulence analysis.

$(x-x_0)/\delta^*_{in}$	Re_θ	Δx^+	Δy^+_w	Δy^+_δ	Δz^+
5077	5200	4.74	0.53	2.48	4.29
6443	8000	4.65	0.52	3.36	4.20
7575	10500	4.54	0.51	4.08	4.10

3.3 Turbulent regime

Moving further downstream, the flow enters in the fully turbulent region. Statistical quantities are investigated at three locations reported in table 2. A preliminary assessment of the velocity profiles scaling is shown in fig. 8, displaying the classical Van Driest transformation for the streamwise velocity:

$$u^+_{VD} = \frac{1}{u_\tau}\int_0^{\bar{u}} \sqrt{\frac{\overline{\rho}}{\rho_w}}\,\mathrm{d}u \qquad (14)$$

The logarithmic law is well described by $u^+ = \frac{1}{\kappa}\ln(y^+) + C$, with κ=0.41 and C=5.8. Different values for the constant C have been used in literature, ranging from 5.2 to 6.2 [5, 22, 8]; the value 5.8 seems to be suitable in this case. The data are found to better match the logarithmic law as the Reynolds number increases; the higher values in the outer layer encountered when moving further downstream are due to the decreasing trend of the friction velocity u_τ. Figure 9 reports the profiles of the Damköhler number $\mathrm{Da}_n = \overline{\dot{\omega}_n/\rho}\;\overline{\mu_w}/\overline{\tau_w}$, which is a measure of the ratio between the flow residence times and the chemical relaxation times. Small values of Da_n imply that chemical dissociation is slower than the characteristic time scale of the flow and the monotonic trend highlights that the maximum chemical activity is close to the wall. Furthermore, the profiles at lower Re_θ exhibit slightly higher values in magnitude. Globally, the Reynolds stresses (shown in fig. 10(a) in inner scaling) confirm previous observations [8] stating that the influence of chemical reactions on the kinematic field is small. Of note, the semi-local transformation introduced in Trettel & Larsson's work [30] allows a better collapse in the viscous sublayer but does not improve the scaling further from the wall. Temperature fluctuations, shown in figure 10(b), exhibit a peak at the end of the logarithmic zone which is more marked for the transitional profiles. Even though the maximum temperature is located at the wall, the large r.m.s. and mean values of the temperature in the buffer layer lead to a peak in the species production / destruction, confirmed by inspection of fig. 11. In this figure, molecular nitrogen fluctuations are not shown since their values are two order of magnitude smaller than the other species. The location at the lowest Reynolds number exhibit intermediate value of the fluctuations; afterwards, at $Re_\theta = 8000$, the fluctuations tend to decrease before and then reach the largest value at the last streamwise position. This highlights the activity of finite-rate

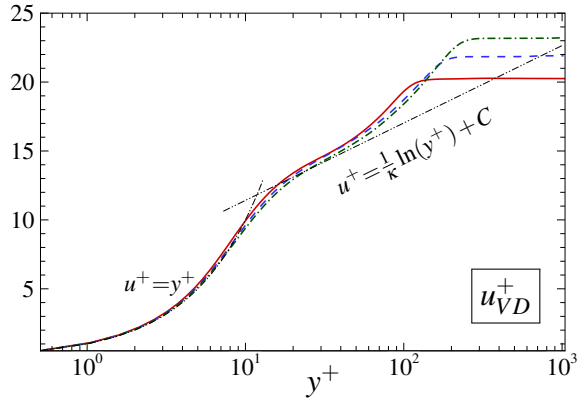

Figure 8: Wall-normal profiles of the van Driest-transformed streamwise velocity; (——) $Re_\theta = 5200$, (- - - -) $Re_\theta = 8000$, (-·-·-·-) $Re_\theta = 10500$.

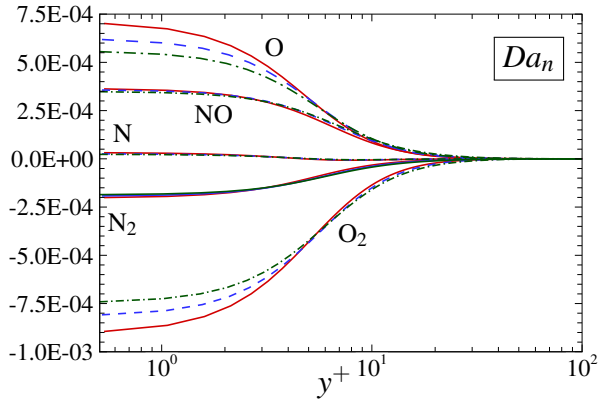

Figure 9: Evolution of the Damköhler number, in inner scaling; (——) $Re_\theta = 5200$; (- - - -) $Re_\theta = 8000$, (-·-·-·-) $Re_\theta = 10500$.

chemistry, since species mass fractions do not directly follow the temperature trend.

4. CONCLUSIONS

High-enthalpy effects on compressible wall-bounded turbulent flows have been analyzed by means of direct numerical simulations of a hypersonic, chemically out-of-equilibrium turbulent boundary layer. The novelty of this work lies in a complete analysis of one of the few existing spatially-developing boundary layers with finite-rate chemistry, encompassing laminar-to-turbulence breakdown as well. The free-stream thermodynamic conditions, albeit not representative of any physical re-entry trajectory or trans-atmospheric flight, are chosen to match those of a configuration largely analyzed in previous stability studies; specifically, a nominal Mach number of 10 and a free-stream temperature of 350 K. The temperatures reached in the boundary layer are such that gas dissociation phenomena occur, giving rise to a non-

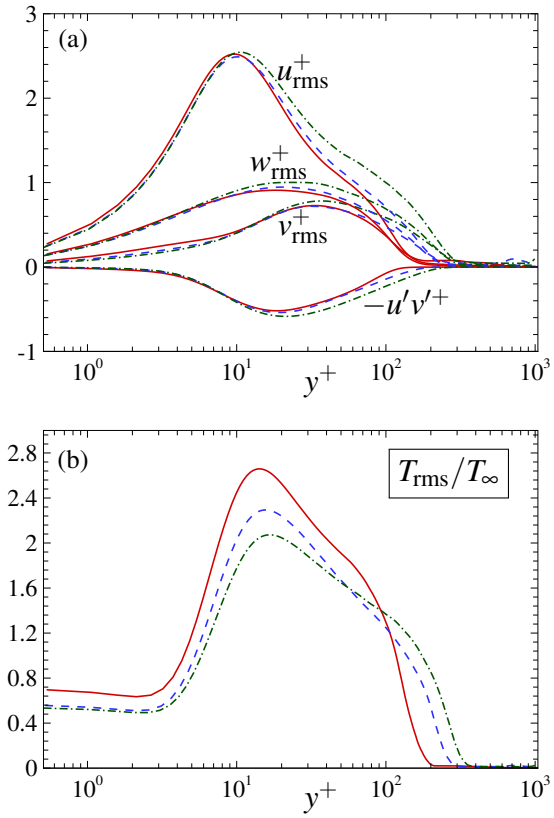

Figure 10: Wall-normal profiles velocity fluctuations (a) and temperature fluctuations (b), in inner scaling; (——) $Re_\theta = 5200$, (- - - -) $Re_\theta = 8000$, (-·-·-·-) $Re_\theta = 10500$.

equilibrium chemical state. The influence of these high-enthalpy effects on laminar, transitional and turbulent region is investigated.

Wall quantities such as the skin friction coefficient, mean temperature and species mass fractions are analysed and compared to the local self-similar solution in the first portion of the domain. The profiles follow the same trend of the similarity results, even though discrepancies are present due to the hypothesis of null pressure gradient in the boundary layer equations set. As the reacting mixture evolves along the plate, oxygen is partially dissociated, but the equilibrium composition is never reached. A modal analysis based on the maximum streamwise velocity fluctuations points out that the mechanism responsible for the breakdown is the second mode fundamental resonance. This scenario leads to a late transition and to the growth of streaks modes once that the two-dimensional mode saturates; transition is observed at a very short distance downstream of the streak appearance. Mean and fluctuating statistics reveal that chemical activity is mostly located between the plate wall and the buffer layer region, although the chemical time scales are much smaller than flow residence time scale throughout the flow. Fluctuations of species mass fractions exhibit

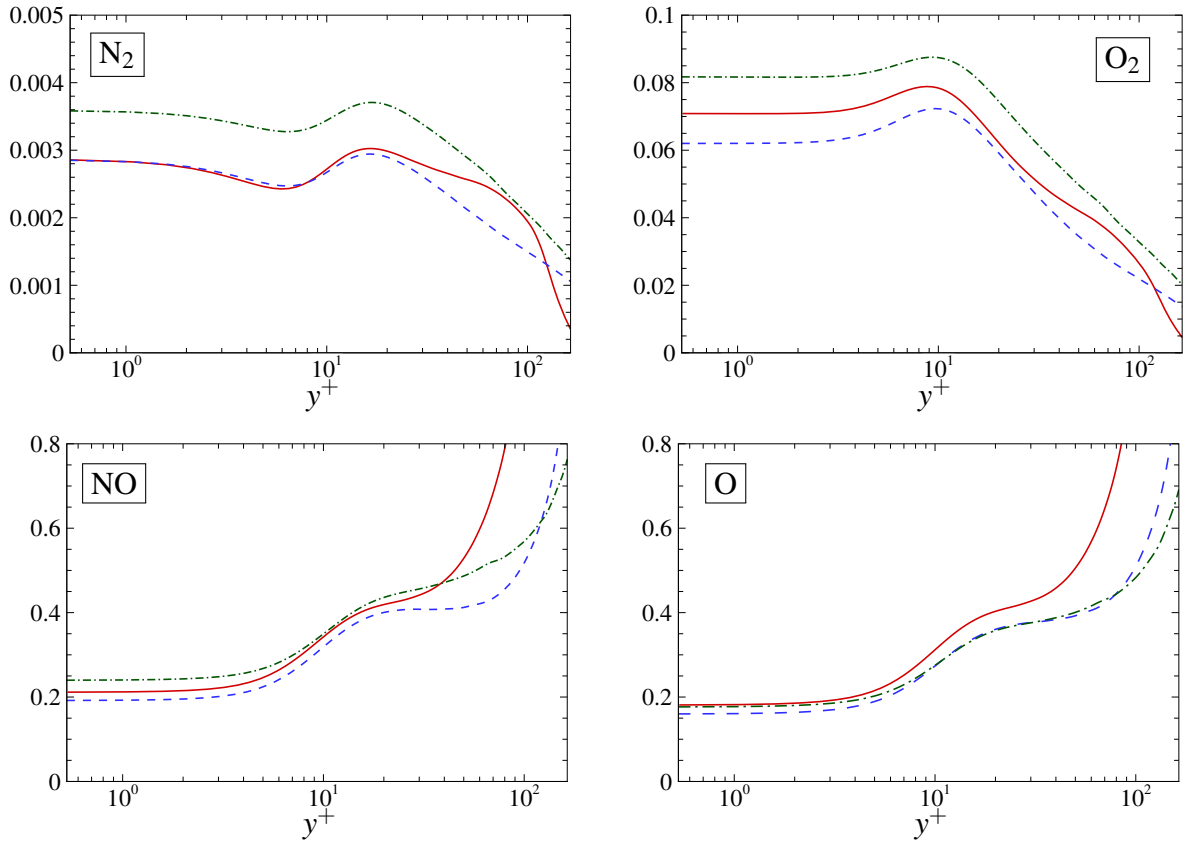

Figure 11: Relative fluctuating quantities of species mass fractions $(Y_{\mathrm{rms}}/\overline{Y})_{\mathrm{n}}$; (——) $Re_\theta = 5200$, (- - - -) $Re_\theta = 8000$, (-·-·-·-) $Re_\theta = 10500$. $(Y_{\mathrm{rms}}/\overline{Y})_{\mathrm{N}}$ is not shown due to its very low values.

a peak in the region of maximum turbulent production, in agreement with the fluctuating profiles of temperature, whereas the trends of the dynamic field are little affected by chemical non-equilibrium.

Since most of the flow features are driven by the wall condition, further investigations are in progress for elucidating the influence of wall cooling. In that case, it is expected that the region of maximum chemical activity moves away from the wall, approaching that of maximum turbulence production and therefore enhancing the turbulence-chemistry interactions. Thermal non-equilibrium conditions will be considered as well, with the aim of quantifying the influence of thermal relaxation phenomena on wall turbulence dynamics.

5. ACKNOWLEDGMENTS

This work was granted access to the HPC resources of IDRIS and TGCC under the allocation A0072B10947 made by GENCI (Grand Equipement National de Calcul Intensif). We also acknowledge CINECA for awarding access to the Galileo supercomputer under the allocation HP10CLMXP0.

REFERENCES

[1] J. D. Anderson. *Hypersonic and high temeprature gas dynamics*. American Institute of Aeronautics and Astronautics, 2006.

[2] J. J. Bertin and R. M. Cummings. Critical hypersonic aerothermodynamic phenomena. *Annu. Rev. Fluid Mech.*, 38:129–157, 2006.

[3] A. Bhagatwala and S.K. Lele. A modified artificial viscosity approach for compressible turbulence simulations. *Journal of Computational Physics*, 228(14):4965–4969, 2009.

[4] F. G. Blottner. Chemically reacting viscous flow program for multi-component gas mixtures. 1971.

[5] Peter Bradshaw. Compressible turbulent shear layers. *Annual Review of Fluid Mechanics*, 9(1):33–52, 1977.

[6] G. Candler. Rate effects in hypersonic flows. *Annual review of Fluid Mechanics*, 51:379–402, 2019.

[7] L. Duan, I. Beekman, and M. P. Martín. Direct numerical simulation of hypersonic turbulent bound-

ary layers. Part 2. Effect of wall temperature. *Journal of Fluid Mechanics*, 655:419–445, 2010.

[8] L. Duan and M. P. Martín. Direct numerical simulation of hypersonic turbulent boundary layers. Part 4. Effect of high enthalpy. *Journal of Fluid Mechanics*, 684:25–59, 2011.

[9] L. Duan, P. Martín, and I. Beekman. Direct numerical simulation of hypersonic turbulent boundary layers with varying freestream Mach number. In *48th AIAA Aerospace Sciences Meeting Including the New Horizons Forum and Aerospace Exposition*, page 353, 2010.

[10] F. Ducros, V. Ferrand, F. Nicoud, C. Weber, D. Darracq, C. Gacherieu, and T. Poinsot. Large-eddy simulation of the shock/turbulence interaction. *Journal of Computational Physics*, 152(2):517–549, 1999.

[11] K. J. Franko, R. MacCormack, and S. K. Lele. Effects of chemistry modeling on hypersonic boundary layer linear stability prediction. In *40th Fluid Dynamics Conference and Exhibit*, page 4601, 2010.

[12] K.J. Franko and S.K. Lele. Breakdown mechanisms and heat transfer overshoot in hypersonic zero pressure gradient boundary layers. *Journal of Fluid Mechanics*, 730:491–532, 2013.

[13] Xavier Gloerfelt and J-C Robinet. Silent inflow condition for turbulent boundary layers. *Physical Review Fluids*, 2(12):124603, 2017.

[14] P. A. Gnoffo, R. N. Gupta, and J. L. Shinn. Conservation equations and physical models for hypersonic air flows in thermal and chemical nonequilibrium. 1989.

[15] S. Gottlieb and C.-W. Shu. Total variation diminishing runge-kutta schemes. *Mathematics of computation*, 67(221):73–85, 1998.

[16] R. N. Gupta, J. M. Yos, R. A. Thompson, and KP Lee. A review of reaction rates and thermodynamic and transport properties for an 11-species air model for chemical and thermal nonequilibrium calculations to 30000 K. 1990.

[17] J. Huang, G. L. Nicholson, L. Duan, M. M. Choudhari, and R. D. Bowersox. Simulation and modeling of cold-wall hypersonic turbulent boundary layers on flat plate. In *AIAA Scitech 2020 Forum*, page 0571, 2020.

[18] Mary L Hudson, Ndaona Chokani, and Graham V Candler. Linear stability of hypersonic flow in thermochemical nonequilibrium. *AIAA journal*, 35(6):958–964, 1997.

[19] A. Jameson, W. Schmidt, and E. Turkel. Numerical solutions of the Euler equations by finite volume methods using Runge-Kutta time-stepping schemes. *AIAA Journal*, 81(1259), 1981.

[20] M. Lagha, J. Kim, J. D. Eldredge, and X. Zhong. A numerical study of compressible turbulent boundary layers. *Physics of fluids*, 23(1):015106, 2011.

[21] L. Lees. Laminar heat transfer over blunt-nosed bodies at hypersonic flight speeds. *Journal of Jet Propulsion*, 26(4):259–269, 1956.

[22] Thierry Maeder. *Numerical investigation of supersonic turbulent boundary layers*, volume 394. ETH Zurich, 2000.

[23] M. R. Malik and E. C. Anderson. Real gas effects on hypersonic boundary-layer stability. *Physics of Fluids A: Fluid Dynamics*, 3(5):803–821, 1991.

[24] O. Marxen, G. Iaccarino, and T. E. Magin. Direct numerical simulations of hypersonic boundary-layer transition with finite-rate chemistry. *Journal of Fluid Mechanics*, 755:35–49, 2014.

[25] O. Marxen, T. Magin, G. Iaccarino, and E. Shaqfeh. A high-order numerical method to study hypersonic boundary-layer instability including high-temperature gas effects. *Physics of Fluids*, 23(8):084108, 2011.

[26] F. Miró Miró, F. Pinna, E. S. Beyak, P. Barbante, and H. L. Reed. Diffusion and chemical non-equilibrium effects on hypersonic boundary-layer stability. In *2018 AIAA Aerospace Sciences Meeting*, page 1824, 2018.

[27] C. Park. Assessment of two-temperature kinetic model for ionizing air. *Journal of Thermophysics and Heat Transfer*, 3(3):233–244, 1989.

[28] Thierry Poinsot and Denis Veynante. *Theoretical and numerical combustion*. RT Edwards, Inc., 2005.

[29] C. Roy and F. Blottner. Review and assessment of turbulence models for hypersonic flows. *Progress in aerospace sciences*, 42:469–530, 2006.

[30] A. Trettel and J. Larsson. Mean velocity scaling for compressible wall turbulence with heat transfer. *Physics of Fluids*, 28(2):026102, 2016.

[31] C. Zhang, L. Duan, and M. M. Choudhari. Direct numerical simulation database for supersonic and hypersonic turbulent boundary layers. *AIAA Journal*, 56(11):4297–4311, 2018.